XANES ANALYSIS OF IRON IN ZIRCALOY-4 OXIDES FORMED AT DIFFERENT TEMPERATURES STUDIED WITH MICROBEAM SYNCHROTRON RADIATION

BRENDAN M. ENSOR*, ARTHUR T. MOTTA
Department of Mechanical and Nuclear Engineering, The Pennsylvania State University
227 Reber Building, University Park, PA 16802 – USA

RAM BAJAJ, JOHN R. SEIDENSTICKER
Bettis Atomic Power Laboratory, Bechtel Marine Propulsion Corporation
814 Pittsburgh-McKeesport Boulevard, West Mifflin, PA 15122 – USA

ZHONGHOU CAI
Advanced Photon Source, Argonne National Laboratory
9700 South Cass Avenue, Argonne, IL 60439 – USA

*Corresponding Author - *Email Address:* bme133@psu.edu *Phone*: 814-865-9709

ABSTRACT

The different corrosion rates observed in zirconium alloys are attributed to differences in alloying element content and how these elements affect the microstructure of the protective oxide layers formed in these alloys. In this study, six thin oxide layer samples formed on Zircaloy-4 at four autoclave corrosion temperatures between 274°C and 400°C were examined using a microbeam at the Advanced Photon Source (APS) in Argonne National Laboratory (with 0.2 µm resolution) to perform fluorescence and X-ray absorption near-edge spectroscopy (XANES). The X-ray fluorescence capabilities and high spatial resolution permitted by the microbeam allowed for detailed analysis of the microstructure of the oxide layers to give insight into the growth mechanism of these oxides. Because second-phase precipitates are known to strongly affect overall corrosion behavior, it is important to better understand their oxidation kinetics when incorporated into the oxide layer. To that end, the iron X-ray absorption edge was analyzed using XANES. The results show that zirconium corrodes preferentially compared to iron both in precipitates and in the matrix, with iron atoms becoming completely oxidized ~2 µm from the oxide metal interface in samples corroded in water, and slightly farther in samples corroded in steam.

1. Introduction and Background

Zirconium alloys are widely used in water-cooled nuclear reactors as fuel cladding due to their low neutron cross-section, suitable mechanical properties, and excellent corrosion resistance. Corrosion resistance in these alloys is important because a typical nuclear reactor operates in water at temperatures and pressures as high as 360°C and 15.5 MPa, respectively. These alloys must remain in these harsh environmental conditions for years and, therefore, the fuel cladding, which encapsulates the fuel, must be as resistant to corrosion as practically possible. This is because as zirconium alloys oxidize, in addition to decreased heat transfer through the greater thermal resistance of the oxide layer, hydrogen from the corrosion reaction ingresses into the metal where it may precipitate as hydrides causing embrittlement [1].

Early testing from the 50's and 60's demonstrated that unalloyed zirconium metal, made from crystal bar or sponge exposed to high temperature, exhibits a deleterious oxidation behavior, known as breakaway corrosion, in high temperature water conditions, where accelerated corrosion and oxide spalling occur [2-3]. What makes zirconium alloys more resistant to corrosion

than pure material is the intentional addition of small amounts of alloying elements to the material. Although alloying elements exist in crystal bar and sponge zirconium, their levels are low and they are not properly controlled. Because some alloying elements suppress accelerated corrosion (e.g. Fe), it is logical that studying the behavior of the alloying elements themselves when incorporated into the protective oxide layer can lead to insights into the corrosion of zirconium alloys.

The common commercial zirconium alloys in use today contain tin, niobium, iron, chromium, and nickel, although other elements, including oxygen, have been used [1]. Whereas niobium and tin have reasonable solubility in alpha Zr, the transition alloying elements iron, chromium and nickel dissolve only to a few hundred ppm before forming intermetallic precipitates [1]. There is evidence from numerous studies using both transmission electron microscopy (TEM) and X-ray absorption near-edge structure (XANES) analysis that the second phase particles (SPPs) oxidize later than the Zr matrix [4-10]. XANES analysis has been used by other researchers to determine chemical state, measure atomic distances, and describe local bonding of alloying elements in zirconium alloys [11-13]. Recently, the work of Couet et al. has claimed that Fe and Nb atoms oxidize later than the Zr matrix [4]. The incorporation of second phase particles in the metallic state in the oxide layer could play a role in the oxidation kinetics and hydrogen pickup of the alloy as a whole, since the oxide conductivity and hydrogen transport could be affected by the incorporation of the alloying elements in the metallic state in the oxide layer or by the oxidation of these elements to different oxidation states than those of Zr [4]. Also, the specific role of precipitates in providing cathodic/anodic sites for hydrogen ingress or short circuit paths for electron migration through the oxide would be affected by their oxidation state. In this study, we investigate the oxidation of Fe in zirconium alloy oxide layers as a function of corrosion temperature using microbeam synchrotron radiation, which allows tracking of the evolution of the XANES signal with distance from the metal-oxide interface, in order to understand how temperature plays a role in Fe oxidation.

2. Experimental Methods

2.1. Materials

The alloy of interest for this study was Zircaloy-4, which has a composition of 1.2-1.7 wt.% Sn, 0.18-0.24 wt.% Fe, 0.07-0.13 wt.% Cr, and 1000-1400 ppm oxygen with the remainder as zirconium. The six Zircaloy-4 samples examined in this study are listed in Table 1.

Table 1- Samples examined at the 2-ID-D beamline at the APS

Sample	Alloy	Exposure Condition*	Time (days)	Oxide thickness (μm)**	Heat Treatment [14]
H1190R	Zircaloy-4	274°C water	3003	2.35	β-quenched
N2513	Zircaloy-4	316°C water	3113	13.1	Rx α-annealed
H1405J	Zircaloy-4	360°C water	20	1.14	Rx α-annealed
H1406J	Zircaloy-4	360°C water	120	2.09	Rx α-annealed
H1312J	Zircaloy-4	400°C steam	41.3	3.5	Rx α-annealed
H1313J	Zircaloy-4	400°C steam	259.4	9.1	Rx α-annealed

Five samples in Table 1 were in the recrystallized alpha annealed condition processed in the same manner as described by Bajaj and Kammenzind [14], while the other sample was in the beta quenched and annealed condition and produce smaller precipitates as shown by Anderson and Bajaj [15]. The second phase particles, C14 Laves phase precipitates $Zr(Fe_xCr_y)_2$, in the five alpha annealed Zircaloy-4 samples were intragranularly distributed globular particles that had an

*H1190R, H1312J, and H1313J were corroded for 3 days at 360°C prior to listed exposure, <0.8 μm of the oxide for all
**Oxide thickness is average thickness based on the weight gain of the sample

average diameter of 0.24 µm as described in Kammenzind et al. [16]. The precipitates in the β-quenched sample were of irregular shape and were present at the lath boundaries [15]. Anderson and Bajaj show morphologies, chemical characteristics (Fe/Cr ratio) and crystal structures of the particles for both types of samples [15].

The samples were tested in autoclaves in the form of ~2.5 cm x ~2.5 cm x ~1 mm thick coupons in either single phase water (274-360°C) or steam (400°C) and had film thicknesses ranging from ~1 µm to ~13 µm. Note that some coupons were exposed in the autoclaves in a single exposure run (as short as 20 days) and others multiple exposures to as long as 3113 days. The samples were judiciously selected to study oxidation behavior of Fe in Zircaloy-4 as a function of: (1) exposure temperature from 274°C to 360°C in the same medium (water) in post transition films, (2) environment (water vs. steam), (3) pre-transition vs. near transition film thickness (H1405J at 1.14 µm vs. H1406J at 2.09 µm) at the same temperature in water, (4) same temperature but with different thickness (H1313J and H1312J) in steam, (5) similar exposure times at different temperatures and texture (N2513 vs. H1190R), and (6) same film thickness but different heat treatment (H1190R vs. H1406J), which may reveal different behavior due to differences in particle shapes and chemistries for different heat treatments [15].

Figure 1 shows weight gain (mg/dm^2) vs. exposure time (in days) for the six samples listed in

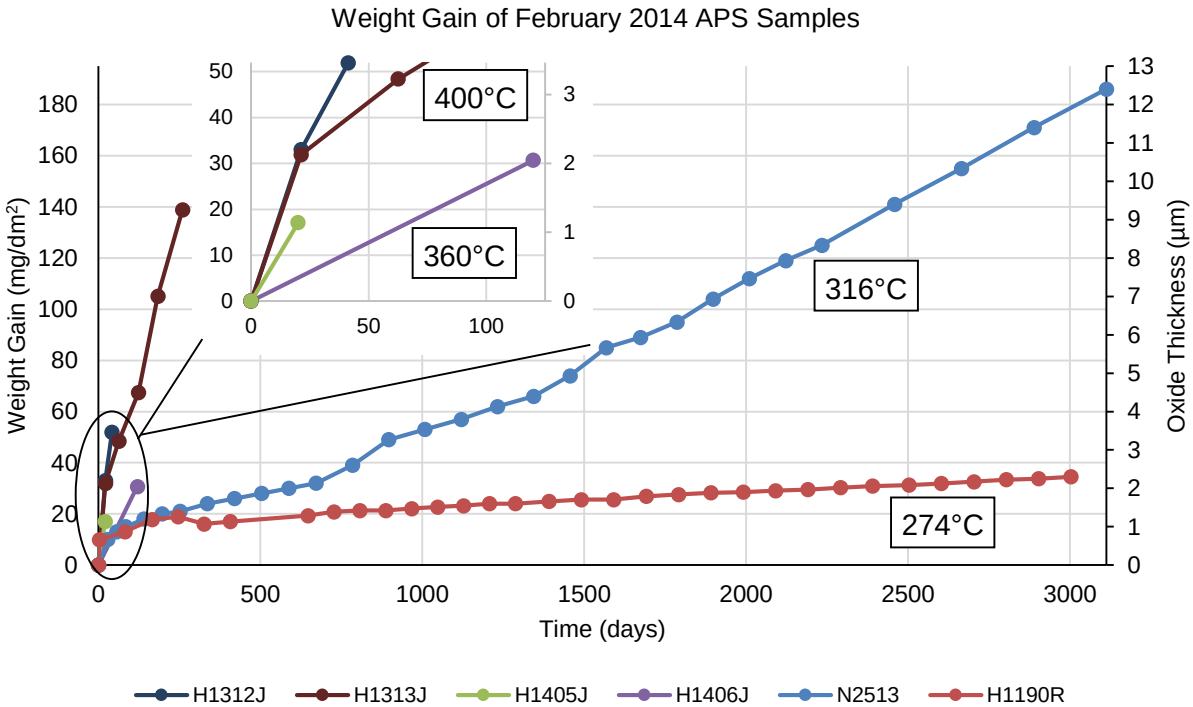

Figure 1- Weight gain data for the six samples examined at the 2-ID-D beamline at the APS in Feb 2014.

Table 1. The average oxide thicknesses are based on the weight gain with a conversion of ~15 mg/dm^2 to 1 µm of oxide. There is a large difference in corrosion rate and exposure times across the samples including samples in both the pre-transition and post-transition regime. Only a few measurements were made for some of the samples corroded over a short time, thus some of the finer aspects of the progression of weight gain were missed.

2.2. Experimental Techniques

The Advanced Photon Source (APS), a national synchrotron radiation light source research facility at the Argonne National Laboratory (ANL), was used to investigate the oxidation behavior of iron

in zirconium alloys corroded at various temperatures. The microdiffraction x-ray source at the APS (2-ID-D beamline) features high beam brilliance, small 0.2 µm x 0.2 µm spot size, and tunable energy from 5 to 32 keV, permitting precise investigation of the Fe x-ray absorption edge using XANES [11-12,17]. The samples were in the form of a segment of the coupon prepared by sectioning, mounting in cross section, and polishing to a final finish in a composite of Mo and epoxy in a brass tube. Sample preparation was identical to that done in Spengler et al. and by other researchers [4,10,18]. At the beamline, each sample was affixed onto an aluminum stud parallel to the beam and then tilted into the beam's path. A Ge(Li) Canberra solid state detector was used to acquire fluorescence data at each step, which allowed precise positioning of the beam relative to the oxide-water and metal-oxide interfaces. Figure 2 shows a fluorescence scan of one of the samples.

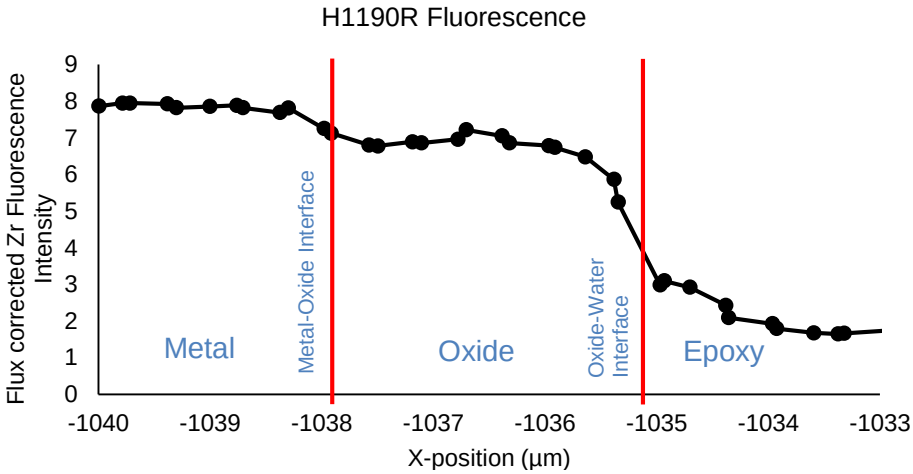

Figure 2- Example of the flux corrected zirconium fluorescence counts from sample H1190R (274°C) taken at the 2-ID-D beamline at the APS used to determine the metal-oxide and oxide-water interfaces.

The Zr fluorescence counts were used to determine the metal-oxide interface and the oxide-water interface. The Zr counts were normalized to the incoming beam flux, which varied slowly during acquisition. The interfaces were then determined by finding the midpoint of the line between the regions on the fluorescence graph, as seen in Figure 2. In Figure 2, on the left, the beam is in the metal; a small drop is seen at the metal-oxide interface (since the oxide provides slightly less Zr fluorescence than the metal) and a larger drop is observed at the oxide-water interface, as indicated. It should be noted that the oxide thickness, measured by fluorescence, does not always match the average oxide thickness based on weight gain due to the variability of the local oxide thickness. Figure 3 shows SEM micrographs of samples corroded in steam (a) and water (b), with

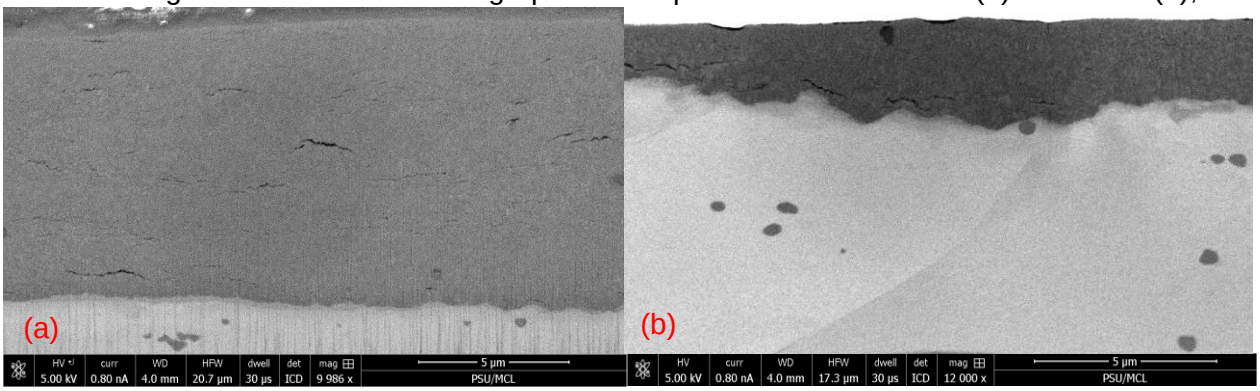

Figure 3- SEM images of (a) H1313J (Zircaloy-4, 400°C for 259.4 days) and (b) H1406J (Zircaloy-4, 360°C for 120 days) taken using a FEI Helios NanoLab™ 660 SEM/FIB showing the oxide (dark gray) and the metal (light gray).

oxide thicknesses of 9.1 µm and 2.09 µm respectively. The oxide layer in (b) illustrates the variability in oxide thickness.

For each scan, the sample was moved in steps of 0.1-0.25 µm across the oxide layer as fluorescence and XANES data were simultaneously acquired. Although the steps were not always equidistant, due to the mechanics of the stage setup and motor, the actual position of the beam was well known. For each sample, one full XANES scan was acquired at each location in the oxide layer. This means that the beam traversed the sample and at each stop a XANES scan near the Fe absorption edge (encompassing a range of 100 eV, from 7.078 keV to 7.178 keV) was obtained. Because XANES examines the structure of the x-ray absorption spectra for a particular element, which is caused by photoabsorption of an electron promoting it to a higher energy state and a subsequent photon emission [17,19], the absorption edge and shape of the spectra are affected by the local bonding of the element in question, providing a means to determine the chemical state of the alloying elements at each location by matching the spectra obtained from a sample to a linear combination of spectra from standards [4,9,13].

The Fe fluorescence counts were used to examine the Fe absorption edge. Examples of the flux-corrected Fe fluorescence counts are shown in Figure 4a. The main point to be observed in Figure

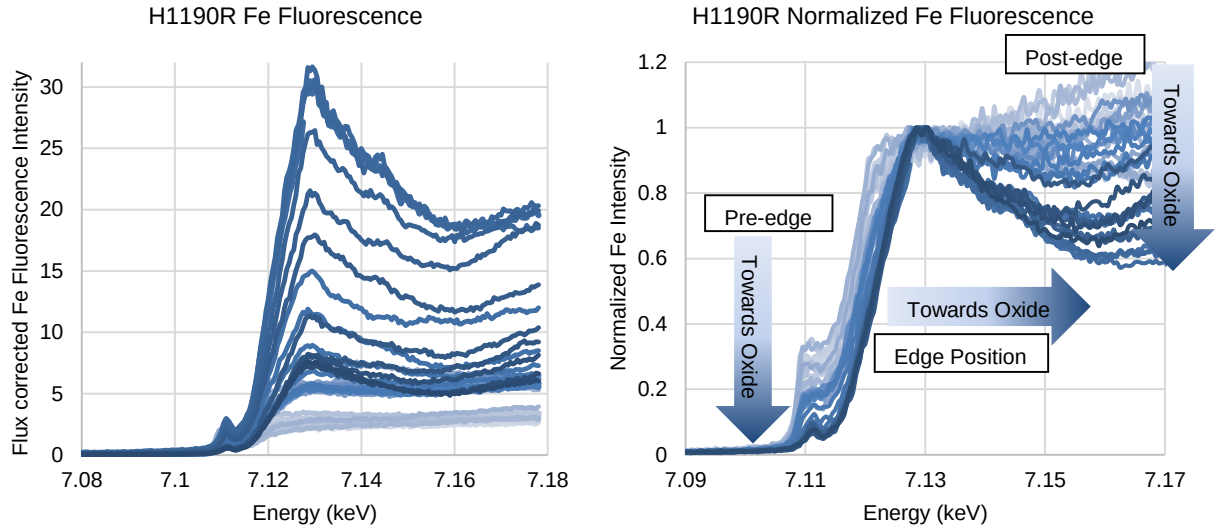

Figure 4- (a) Flux corrected Fe fluorescence counts obtained as the beam is scanned from the metal into the oxide layer cross section for sample H1190R (Zircaloy-4 corroded at 274°C) and (b) normalized to the maximum value between 7.12 and 7.135 keV; examined at the 2-ID-D beamline at the APS.

4a is the change in the shape of the absorption curve as one moves from the metal (lighter) to the oxide (darker lines). Note that the variation in absorption intensity is not physically significant, since it primarily depends on the number of Fe atoms hit by the beam and each spectrum is analyzed individually. Based on a 0.5% volume percentage of precipitates, with an average spherical precipitate diameter of 0.24 µm [14], 0.2 µm x 1 µm footprint of the beam, and at least a 50 µm beam penetration (from mass attenuation of photons at these energies), on average at least four full precipitates are captured in each scan (the four could be composed fractionally of many more than four precipitates). Over the course of a 10 micron scan, there is a >99.7% probability of hitting at least one precipitate at every point [4]. The actual number of precipitates contributing to the signal is higher. The XANES spectra shown in Figure 4a were taken from a 2.35 µm thick oxide formed at 274°C. Here the colors indicate the translation of the microbeam from the metal (lighter lines) into the oxide until the oxide-water interface. Figure 4b shows a normalization of the flux corrected Fe fluorescence intensity shown in Figure 4a. The spectra were normalized to the maximum value for an individual scan between 7.12 keV and 7.135 keV. The spectra acquired from locations in the oxide that are furthest from the metal-oxide interface are darkest. It is clear that a systematic variation of the Fe x-ray absorption edge occurs as one moves

away from the metal-oxide interface through the oxide. Note the evolution of edge energy[1], pre-edge maximum intensity[2], and post-edge minimum intensity[3] in Figure 4b.

It is clear that the XANES spectra evolve considerably as the beam travels across the oxide, but in order to analyze this quantitatively, it is necessary to use standards. Thus, standards of bcc-Fe, Fe_2O_3, Fe_3O_4, Fe in Zircaloy-4, and $Zr(Fe,Cr)_2$ were examined to create fluorescence plots around the Fe absorption edge. Except for Fe in Zircaloy-4, the standards were in the form of powders acquired from Alfa Aesar, used previously in other XANES studies [4]. These standards were normalized in the same manner as described above for Figure 4b. They were then examined using the Demeter software package, part of the Athena Suite [20]. Plots of the standards used can be seen in Figure 5. Note that the edge of the metallic standards is lower in energy than that of the

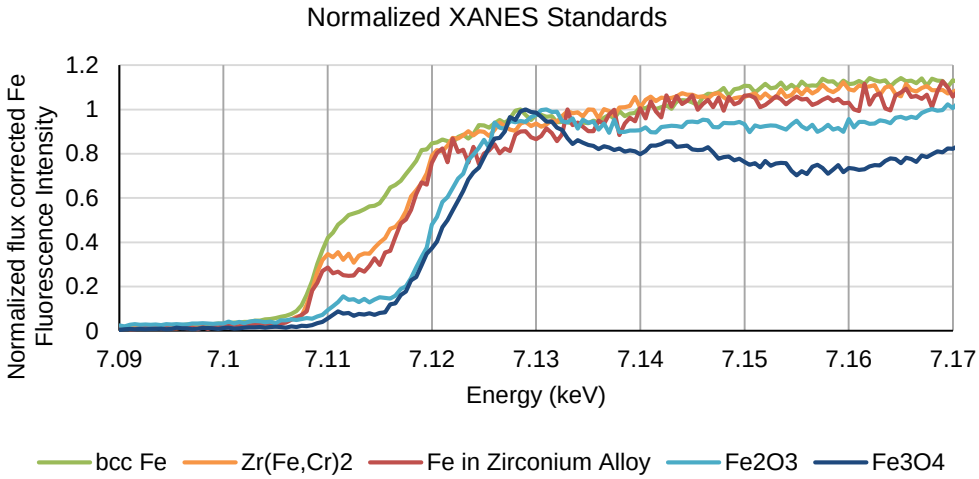

Figure 5- Fe fluorescence data of the standards used to perform XANES on the six samples examined at the 2-ID-D beamline at the APS.

oxidized standards. Also, the pre-edge maximum intensity and the post-edge minimum intensity vary between metallic and oxidized Fe. The differences between individual metallic and oxide standards being less substantial, the focus of the analysis is mostly on the overall sum of oxidized Fe versus metallic Fe.

XANES analysis was performed on oxide layers formed on the six samples shown in Table 1. The fluorescence patterns were fit as a linear combination of the standards to determine how much of the Fe in the alloys was in metallic form (bcc Fe, Fe in Zircaloy-4, and $Zr(Fe,Cr)_2$) or in an oxidized state (Fe_2O_3, and Fe_3O_4). Thus, the best overall fit (as described by Couet et al. [4]) provided our best estimate of the fraction of Fe atoms oxidized at the particular location. The Fe XANES done here cannot determine the difference between Fe in solid solution and that in precipitates. In the oxide, the extent of Fe oxidation is estimated by comparing to powder Fe_2O_3 and Fe_3O_4 standards. Goodness of fit is shown in terms of error bars in the figures produced. Finally, the maximum of the pre-edge peak, the edge position, and post-edge minimum intensities were also analyzed and plotted as a function of distance from the metal-oxide interface to serve as additional indicators of the Fe oxidation process.

3. Results

Figure 6 shows similar data from the oxide layer shown in Figure 4, but showing the different spectra stacked as one moves across the oxide layer for 2 samples, N2513 and H1313J. The shift

[1] The edge position here is defined here as the energy where the normalized Fe counts cross 0.5
[2] The pre-edge maximum intensity here is defined as the maximum of the normalized Fe counts between 7.108 and 7.112 keV
[3] The post-edge minimum intensity here is defined as the minimum of the normalized Fe counts between 7.152 and 7.162 keV

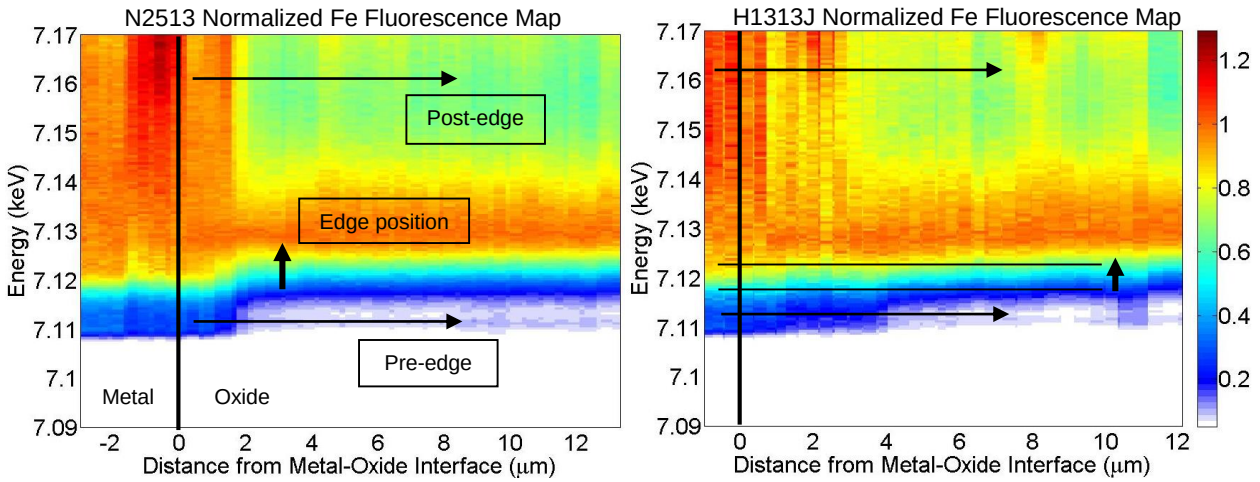

Figure 6- An intensity map of N2513 (Zircaloy-4, 316°C 3113 days) and H1313J (Zircaloy-4, 400°C 259.4 days) showing the movement of the edge position, pre-edge peak intensity, and post-edge minimum as the microbeam travels from the metal-oxide to the oxide-water interface (right most edge of each map)

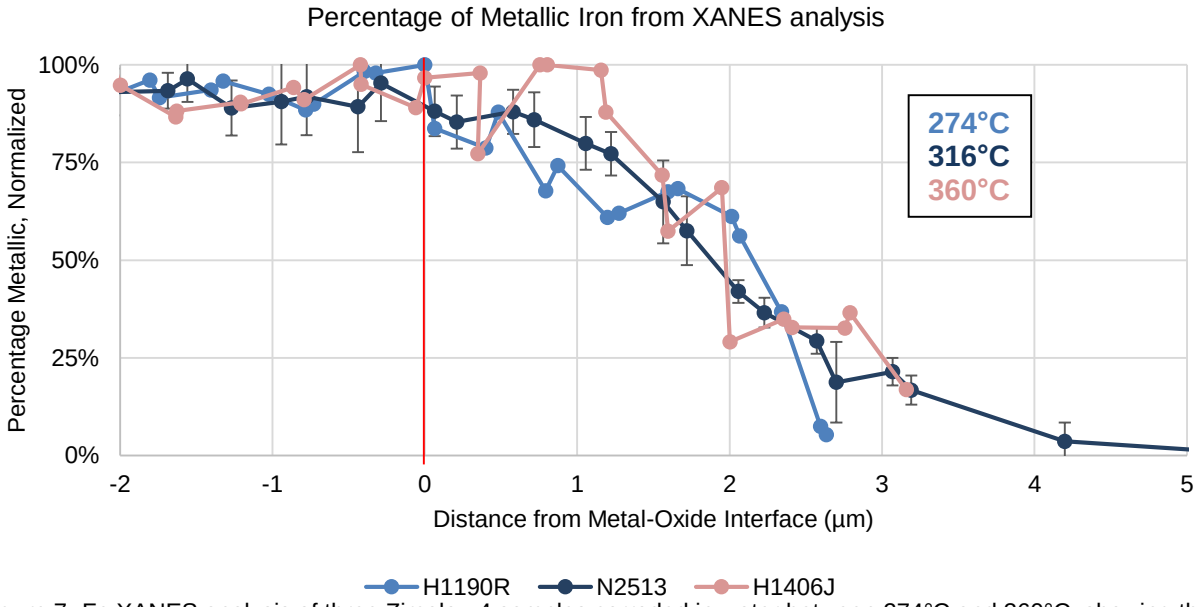

Figure 7- Fe XANES analysis of three Zircaloy-4 samples corroded in water between 274°C and 360°C showing the percentage of the fit to the spectrum data coming from metallic standards, error bars are mostly ≤10% and are shown for N2513 as an example

of the absorption edge to a higher energy value in the oxide is clearly seen. To analyze these results, each individual spectrum is fitted with a linear combination of the standards as described previously [4]. Although the spectra from different oxide and metal phases are difficult to distinguish between each other (e.g. Fe_2O_3 from Fe_3O_4), it is easy to distinguish the oxide phases from the metal (e.g. Fe_2O_3 from $Zr(Fe,Cr)_2$). All the scans were analyzed in this manner and the sum of all the oxide phases in the fits gives the fraction of oxidized iron atoms. Figure 7 shows a comparison between samples corroded in water at different temperatures that have undergone transition (>2 μm oxide), showing a remarkable similarity in behavior. Figure 8 shows a comparison between samples corroded at the same temperature in water (360°C) but at different thicknesses, pre and post-transition. The difference shown is due to the effect of complete oxidation of Fe occurring at the outer oxide edge in contact with the water. Figure 9 compares the samples corroded to a similarly thick oxide (>9 μm) but in different environments, 316°C water vs. 400°C steam. Note the remarkable difference between the steam and water corroded samples.

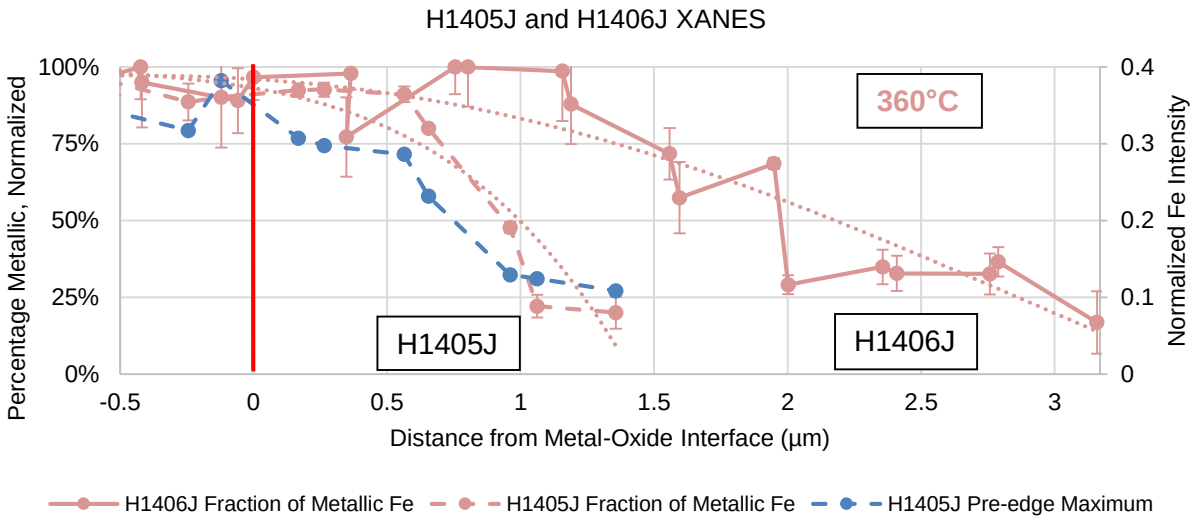

Figure 8- Comparison between H1405 (Zircaloy-4, 360°C 20 days) and H1406J (Zircaloy-4, 360°C 120 days) with the pre-edge maximum intensity of H1405J overlaid

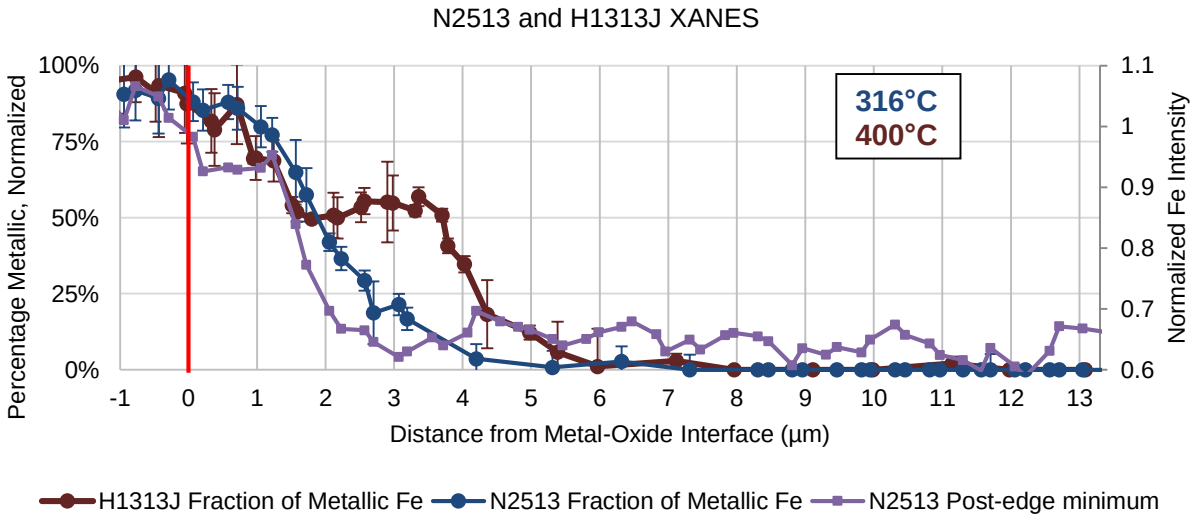

Figure 9- Comparison between N2513 (Zircaloy-4, 316°C water for 3113 days) and H1313J (Zircaloy-4, 400°C steam for 259.4 days) with the post-edge minimum of N2513 overlaid

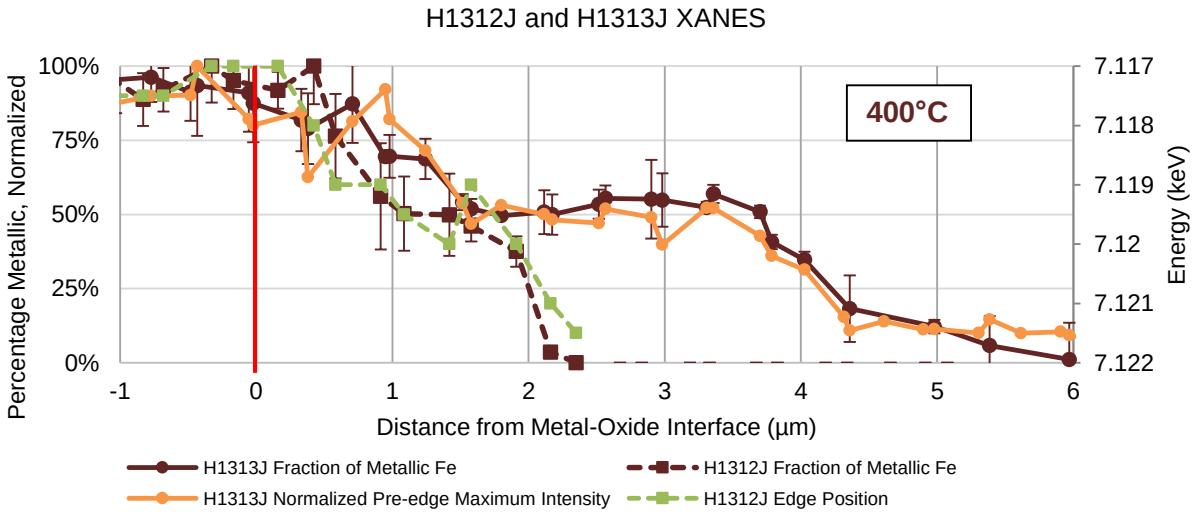

Figure 10- Comparison between H1313J (Zircaloy-4, 400°C steam for 259.4 days) with the pre-edge maximum intensity overlaid and H1312J (Zircaloy-4, 400°C steam for 41.3 days) with the edge position overlaid

Figure 10 shows a comparison between samples corroded at the same temperature in steam (400°C) but at different thicknesses. In these figures the metal-oxide interface is at zero. In the negative region (metal) Fe is completely metallic.

Although we note that a significant degree of scatter exists on the plots indicating some uncertainty on the measurements, at the metal-oxide interface Zr goes from completely unoxidized to completely oxidized, but within the first micron or so this is not true for Fe, which retains a significant metallic fraction. However, looking further into the layer, within ~2 μm of the metal-oxide interface, analysis of the XANES spectra shows that the Fe has been mostly oxidized, showing a metallic fraction less than 50%, and at about ~3 μm, for most cases, Fe is completely oxidized such that the XANES spectra can be fitted entirely using a combination of oxide standards. Comparing the spectra obtained from oxide layers grown at different temperatures, it is possible to note that the complete oxidation of Fe in the samples formed at 400°C appears to take place further away from the metal-oxide interface than in the oxide layers formed at lower temperature. It is possible that differences in oxidation kinetics can account for this behavior, since the faster kinetics at higher temperature would allow the oxide front, the average radial position of the metal-oxide interface, to advance further into the metal before oxidation of Fe would occur. The plateau could also be related to corrosion in steam rather than in water. These results will need to be confirmed with further analysis. Overall, the XANES spectra appear remarkably similar, in spite of the wide difference in exposure times (from 20 to 3113 days), suggesting that the corrosion mechanism does not significantly change over this temperature range.

The analysis of the oxide layers using the other parameters (edge position, pre-edge maximum and post-edge minimum) mostly confirms the analysis above. Figure 10 shows a plot of the edge position plotted versus position in the oxide. It is clear that as the metallic fraction decreases, the edge energy increases. Figure 8 and 10 show the pre-edge maximum, again plotted together with metallic fraction versus position in the oxide. Again, it is clear that the pre-edge maximum decreased in accordance with the decrease in metallic Fe fraction. Finally, Figure 9 shows the post-edge minimum which also follows well the decrease in metallic Fe. The consistency of these results gives further confidence that the analysis is valid.

4. Discussion

As seen in Figures 8-10, the three parameters - pre-edge maximum intensity, absorption edge position, and post-edge minimum – change as the beam moves from the metal through the oxide to the outside edge. This behavior correlates well with the metallic fraction determined from the fitting analysis of the full spectra. The behavior is a result of bonding differences between metallic Fe atoms (either in a precipitate or in solid solution) versus those in Fe_2O_3 and Fe_3O_4. As the Fe atom shares electrons with the oxygen atom, it also becomes more difficult to excite its inner shell electrons. Thus, the edge position moves to a slightly higher energy level. Similarly, the pre-edge peak intensity and post-edge intensity also decrease with increasing oxidation. Therefore, these may be good additional metrics for characterizing the oxidation of alloying elements, especially Fe. In fact this is to be expected, as the XANES analysis that fits the sample spectra to the linear combination of standard spectra is heavily influenced by all three parameters, as seen in Figure 4. The caveat with this method is it does not allow the determination of specific chemical state (oxidation state) of Fe, just a relative measure of how oxidized it has become.

The preferential oxidation of Zr compared to Fe is driven by the oxygen potential across the oxide. Once the oxygen potential has increased enough, there is enough driving force to cause Fe oxidation, as stated previously [6]. When chromium oxidizes at a lower oxygen potential than Fe, the Fe in precipitates forms locally as bcc Fe due to dissolution from the precipitates [5]. The bcc Fe was detected in the samples examined, primarily from the metal-oxide interface up to the point

that the Fe became oxidized. Previous XANES examinations of oxide layers formed on Zr alloys have shown that the point in the oxide where the precipitates are mostly oxidized roughly coincides with the point where interconnected microporosity has reached [4,21].

No change in the oxidation of Fe was observed between the different liquid water corrosion in the temperature ranges studied (274°C-360°C), suggesting that the corrosion process is similar for these temperatures, in spite of the wide differences in exposure times. Despite these similarities, some differences were seen in the distance from the metal-oxide interface for full Fe oxidation in the steam samples. The full Fe oxidation appeared to occur further into the oxide during autoclave corrosion at higher temperature in steam than at lower temperature in water. The much faster kinetics at high temperature (see Figure 1) would leave less time for Fe to oxidize and thus create a non-equilibrium situation where a driving force for Fe oxidation exists, but the actual transformation has not yet occurred. As seen previously by Couet et al. [4], in the spectra of the steam samples, the metallic fraction shows an initial “plateau”, at a lower percentage of metallic Fe than in the metal, suggesting that a fraction of the Fe was oxidized while another population is still metallic. A possible interpretation would be to ascribe the first population to early oxidation of the Fe to the Fe in solid solution and the second population in the plateau to the Fe in precipitates. It is also possible that Fe oxidation during corrosion in steam occurs differently than in water. It would be useful to be able to compare samples corroded in both steam and water at the same temperature to test this, as the effect is observed in a 40°C increase from the 360°C samples, yet no similar change in Fe oxidation behavior is observed from 274°C to 360°C. It also could be that the precipitates oxidize first on the edges, leaving the inside metallic, but this needs to be confirmed by TEM observations. Finally, it is possible that precipitates of different composition (Fe/Cr ratio or possibly Zr_3Fe) corrode at different rates. Additional experiments would need to be performed to confirm the means of the difference in behavior observed in 400°C samples in this study. Because the fraction of metallic Fe in the oxide can affect the oxide electronic conductivity, and this in turn can affect the hydrogen pickup fraction, these different kinetics of oxidation may be important in determining cladding behavior.

5. Conclusions

The oxidation state of Fe within the oxide layers formed in Zircaloy-4, corroded at a range of temperatures (274°C-400°C), was examined using XANES. The XANES spectra of Fe were acquired and analyzed as a function of distance from the metal-oxide interface using synchrotron radiation from the 2-ID-D microbeam at the APS with a spatial resolution of ~ 0.2 µm. The following conclusions resulted from the analysis of the linear combination fits from XANES standards to the XANES data and characteristics of the Fe fluorescence spectra:

- Zirconium oxidizes preferentially with respect to iron as the oxide front advances into the metal, with the fraction of oxidized Fe atoms becoming 100% at about ~2 µm from the metal-oxide interface for water oxidation conditions.
- The overall similarity of the Fe oxidation in water suggests that the corrosion mechanism is similar in this temperature range (274°C-360°C).
- The corrosion temperature does not show a significant effect on Fe oxidation in samples corroded at temperatures from 274°C to 360°C in water, but, a slight difference is seen in the Fe oxidation in samples corroded at 400°C in steam in which the Fe atoms appear completely oxidized at a slightly larger distance from the oxide front than in samples corroded at lower temperatures. This could be caused by the fact that oxidation of the matrix occurs faster at a higher temperature such that the oxide front can travel farther before iron oxidation can occur.
- Additionally, three spectrum parameters – edge position, pre-edge maximum intensity, and post-edge minimum – are identified that match reasonably well with the analysis of the

spectra in determining Fe oxidation and provide additional insight into the behavior of iron as studied by XANES.

Acknowledgements

This research was performed under appointment to the Rickover Fellowship Program in Nuclear Engineering sponsored by Naval Reactors Division of the U.S. Department of Energy (B. Ensor). This research was performed under contract by Bettis Atomic Power Laboratory of the Bechtel Marine Propulsion Corporation. This research used resources of the Advanced Photon Source, a U.S. Department of Energy (DOE) Office of Science User Facility operated for the DOE Office of Science by Argonne National Laboratory under Contract No. DE-AC02-06CH11357. The authors would also like to thank Ashley Lucente of Knolls Atomic Power Laboratory for her role as an adviser and helpful participation in discussions.

References

[1] Lemaignan, C. and A.T. Motta. "Zirconium alloys in nuclear applications." *Materials Science and Technology, A Comprehensive Treatment*. Ed. B.R.T. Frost. Vol. 10B. VCH, (1994): 1 - 51.

[2] Cox, B. "Some thoughts on the mechanisms of in-reactor corrosion of zirconium alloys." *Journal of Nuclear Materials* 336 (2005): 331-368.

[3] Ahmed, T. and L. H. Keys. "The breakaway oxidation of zirconium and its alloys a review." *Journal of the Less-Common Metals* 39 (1975): 99-107.

[4] Couet, Adrien, et al. "Microbeam X-ray absorption near-edge spectroscopy study of the oxidation of Fe and Nb in zirconium alloy oxide layers." *Journal of Nuclear Materials* 452 (2014): 614-627.

[5] Pecheur, Dominique, et al. "Oxidation of intermetallic precipitates in ZIrcaloy-4: Impact of irradiation." *Zirconium in the Nuclear Industry: Tenth International Symposium, ASTM STP 1245*. Ed. A. M. Garde and E. R. Bradley. Philadelphia: American Society for Testing and Materials, (1994): 687-708.

[6] Pecheur, D., et al. "Precipitate evolution in the Zircaloy-4 oxide layer." *Journal of Nuclear Materials* 189 (1992): 318-332.

[7] Hatano, Yuji, et al. "Role of intermetallic precipitates in hydrogen transport through oxide films on Zircaloy." *Zirconium in the Nuclear Industry: Twelfth International Symposium, ASTM STP 1354*. Ed. G. P. Sabol and G. D. Moan. West Conshohocken, PA: American Society for Testing and Materials, (2000): 901-917.

[8] de Gabory, Benoit, Arthur T. Motta and Ke Wang. "Transmission electron microscopy characterization of Zircaloy-4 and ZIRLO oxide layers." *Journal of Nuclear Materials* 456 (2015): 272-280.

[9] Sakamoto, Ken, Katsumi Une and Masaki Aomi. "Chemical state of alloying elements in oxide layer." *2010 LWR Fuel Performance, TopFuel 2010*. Orlando, (2010): 101-106.

[10] Yilmazbayhan, Aylin, et al. "Transmission electron microscopy examination of oxide layers formed on Zr alloys." *Journal of Nuclear Materials* 349 (2006): 265-281.

[11] Degueldre, C., et al. "Nuclear material investigations by advanced analytical techniques." *Nuclear Instruments and Methods in Physics Research B* 268 (2010): 3364-3370.

[12] Degueldre, C., et al. "Zircaloy-2 secondary phase precipitate analysis by X-ray microspectroscopy." *Talanta* 75 (2008): 402-406 [13] Bianconi, Antonio. "Surface X-ray absorption spectroscopy: surface EXAFS and surface XANES." *Applications of Surface Science* 6 (1980): 392-418.

[13] Sakamoto, K., et al. "Depth profile of chemical states of alloying elements in oxide layer of Zr-based alloys." *Progress in Nuclear Energy* 57 (2012): 101-105.

[14] Bajaj, R., B. F. Kammenzind, and D. Farkas, "Effects of neutron irradiation on the microstructure of alpha-annealed Zircaloy-4." *Zirconium in the Nuclear Industry: Thirteenth International Symposium, ASTM STP 1423*. G. D. Moan and P. Rudling, Eds., West Conshohocken, PA: American Society for Testing and Materials, (2002): 400-426.
[15] Anderson, Ken. R. and Ram Bajaj, “Microstructural and microchemical analyses of extracted second-phase precipitates in alpha-annealed and beta-quenched Zircaloy-4.” *Microscopy ad Microanalysis*, 20 (Suppl. 3), (2014): 500-501.
[16] Kammenzind, B. F., K. L. Eklund, and R. Bajaj, "The influence of in-situ clad straining on the corrosion of Zircaloy in a PWR water environment." *Zirconium in the Nuclear Industry: Thirteenth International Symposium, ASTM STP 1423*. G. D. Moan and P. Rudling, Eds., West Conshohocken, PA: American Society for Testing and Materials, (2002): 524-560.
[17] Eisenberger, P. and B.M. Kincaid. "EXAFS: New Horizons in Structure Determinations." *Science* 200 (1978): 1441-1447.
[18] Spengler, David J., et al. "Characterization of Zircaloy-4 corrosion films using microbeam synchrotron radiation." *Journal of Nuclear Materials* 464 (2015): 107-118.
[19] Bianconi, Antonio. "Surface X-ray absorption spectroscopy: surface EXAFS and surface XANES." *Applications of Surface Science* 6 (1980): 392-418.
[20] Ravel, B. and M. Newville. "Athena, Artemis, Hephaestus: data analysis for X-ray absorption spectroscopy using IFEFFIT." *Journal of Synchrotron Radiation* 12 (2005): 537-541.
[21] Ni, N., et al. “Porosity in oxides on zirconium fuel cladding alloys, and its importance in controlling oxidation rates” Scripta Mater. 62 (2010) 564–567.